Preheating Temperature Control and Low-Contrast Imaging Data Analytics for Laser Powder Bed Fusion

Tianyu Jiang, Mengying Leng, and Xu Chen, *Member, IEEE,*

***Abstract*—Laser powder bed fusion additive manufacturing has seen widespread use for its unique advantages in achievable part complexity and processable materials. However, greater applications of this technique remain hindered by the insufficient assurance of part qualities. A major barrier to such a long-felt but not fully realized quality assurance arises from challenges in sensing and model-based control, particularly when involving materials showing low contrast under laser radiation. This paper presents two advances that contribute to this vista. We (1) propose a model-based multi-zone heating control for minimizing the powder-bed temperature deviation in the presence of part-geometry-induced cross-layer thermal disturbances and (2) create an image analytics framework for process monitoring of low-contrast material LPBF with visible light cameras. The proposed methods are developed and verified on an in-house built feedback-centric laser powder bed fusion platform.**

***Index Terms*—Additive manufacturing, laser powder bed fusion, process monitoring, model-based control, infrared heating, image processing, quality assurance.**

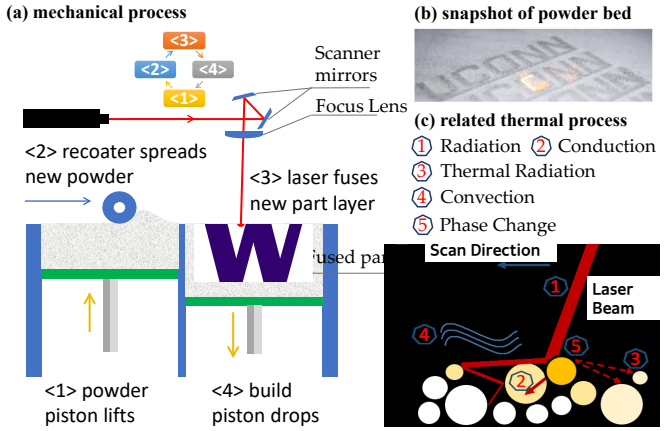

Fig. 1. Illustration of the LPBF process.

I. Introduction

Laser powder bed fusion (LPBF) is one of the additive manufacturing (AM) (also known as three-dimensional (3D) printing) processes, where 3D objects are built from thin layers of materials. During the processing of each layer, a laser beam forms a melt pool that moves at several meters per second to sinter/melt the powder particles (Fig. 1(b)). After consolidation, the powder bed is lowered by the thickness of a single layer. The new powder is then spread over the current deposit to start the next repetition (Fig. 1(a)). Since its first invention and commercialization, LPBF has demonstrated wide-ranging competitive advantages over conventional manufacturing methods. However, limited reliability and reproducibility are hindering broader adoption of this manufacturing technology, especially in such industries as medical devices and aviation [1]–[3].

A critical step to addressing the quality assurance problem is the development of effective real-time monitoring and closed-loop feedback controls [4]. In LPBF, the physics of the non-contact energy deposition is a complicated union of thermal balance, phase change, and solid mechanics (Fig. 1(c)). Pre-process high-fidelity simulations can map out an initial parameter space, and post-process material analyses can reveal the internal quality of the built parts. However, mitigation of various in-process disturbances and uncertainties ultimately hinges on real-time in-process controls [4]–[6]. This has been a long-felt but not realized vista, due to obstacles including (1) the closed architecture of the commercial LPBF machines, (2) the lack of real-time control-oriented modeling, and (3) the need for efficient interpretation and utilization of the monitoring data. This work contributes to address obstacles (2) and (3) towards a quality-assured LPBF.

First, we propose a model-based multi-zone heating control method for minimizing the powder-bed temperature deviation in polymer LPBF in the presence of part-geometry-induced cross-layer thermal disturbance. In LPBF, inhomogeneous shrinkage, warpage, in-build curling, and microstructural inhomogeneities are common problems [3]. These defects are greatly influenced by the inhomogeneous temperature distribution on the powder bed surface. The heating-cooling cycle of previously fused layers is a significant source of such inhomogeneity. The conducted heat from previous layers shapes the temperature profile of the surface layer. For example, when the part has an overhang structure, the temperature within the previously fused area is higher than the powder-supported area, leading to inconsistent melt pool behavior and surface quality on the overhang plane [7].

The existing preheating method utilizes the average temperature measurement of the powder bed as the feedback to control the power of the radiant heater [8], [9]. The shortcoming is that there is no consideration for the temperature distribution of the powder bed. In [9], it is reported

Tianyu Jiang (email: tjiang19@uw.edu), Mengying Leng (email: lengmy19@uw.edu), and Xu Chen (email: chx@uw.edu) are with the Department of Mechanical Engineering, University of Washington, Seattle, WA, 98195, USA.

that the resulting temperature deviation of the powder bed is significant even without cross-layer thermal disturbance. Stepping away from existing LPBF design, this paper develops a novel multi-zone infrared (IR) heating process. Specifically, we create a multi-input multi-output (MIMO) closed-loop heating design, develop a control-oriented model, and propose a new multi-zone heating algorithm. Compared with the state-of-the-art method in the presence of different cross-layer thermal disturbances, the proposed method provides elevated performance similar to results from a model predictive control (MPC) method in a commercial control toolkit. We also demonstrate the flexibility of the proposed design by incorporating an add-on parameter tuning scheme that is adaptive to the thermal disturbance profile.

The second contribution is an image analytics framework for the monitoring of low melt pool contrast material LPBF using visible light cameras. In metal AM, due to the significant temperature differences between the melt pool and the unprocessed loose powder, a simple pixel-level thresholding algorithm is sufficient for identifying the melt isotherm [10]–[12]. However, such a distinction is not available in LPBF of low melt temperature materials, including polymer and composite/coated powders (e.g., glass-filled nylon) [13]. For such applications, substantial work based on infrared cameras has been reported, but a systematic framework on process zone identification, signature extraction, and defect detection using visible light cameras remains underdeveloped. Compared with the IR camera, the visible light camera has several unique advantages for real-time control of LPBF, including (1) higher frame rate and resolution, (2) straightforward employment in coaxial monitoring setup[1], and (3) significantly lower cost.

With the benefits of visible light cameras on the one hand and challenges of data analytics on the other, this paper presents an efficient workflow for extracting important information that reflects the multi-physics evolution of the melt pool, laser-material interaction characteristics, and potential process imperfections. Targeting first at addressing such raw-image issues as noises, inconsistent illumination, and low contrast of the processed zone, we propose to utilize a combination of pre-processing algorithms including the morphological operation, imaging field correction, and adaptive histogram equalization. Utilizing a graph-based segmentation, this approach isolates the area that is processed by the laser source (heat-affected zone). With the segmentation results, we further present the detection of a discontinuity defect and the estimation of the melt pool width for real-time closed-loop control.

The remainder of the paper is organized as follows. Section II describes an in-house developed platform on which this study was performed. Section III presents the powder bed preheating control, following the image analytics framework in Section IV. Section V concludes this paper.

II. Experiment Platform

This work is performed on an in-house developed feedback control-centric polymer LPBF platform. Fig. 2 provides an overview and subsystems of the developed platform. The testbed follows the hardware architecture of industrial LPBF machines (Fig. 1(a)). Table I summarizes the general technical specifications of the testbed.

[1]IR camera usually requires a wide range of wavelength to calculate the object temperature, which makes optical system design challenging.

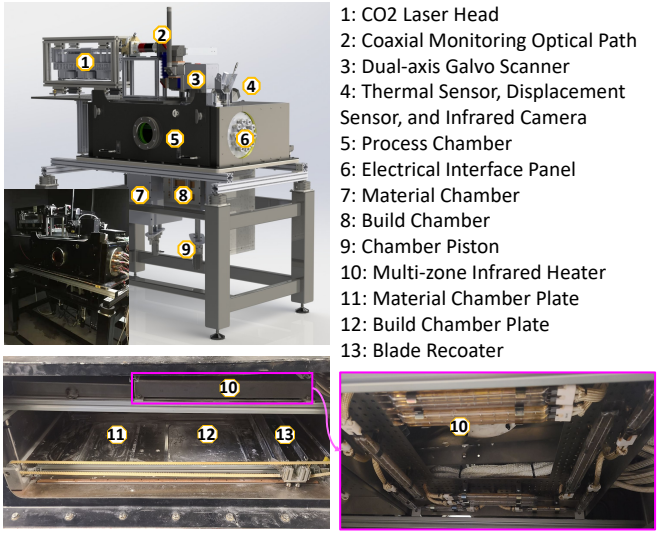

Fig. 2. In-house developed LPBF testbed.

TABLE I
General Technical Specifications of the Developed Polymer LPBF Testbed

Material	polymer (PA12, PEEK, etc.)
Effective building volume	250 × 250 × 150 mm
Feed volume	250 × 178 × 300 mm
Layer thickness	10 μm and above
Laser type	100-watt CO_2 laser, 10.6 μm wavelength
Scan speed	up to 10 m/s
Build plate temperature	up to 300 °C
Process chamber temperature	up to 200 °C
System controller	host computer and NI cRIO-9035
Scanning controller	Scanlab RTC5 control board
Software	in-house developed LabVIEW® program

The platform features various sensors and actuators, thereby allowing closed-loop control for multiple process parameters such as powder-bed temperature, build-chamber temperature, laser power, and scan velocity. The results presented in this paper are based on two control-oriented features described below.

A. Multi-zone Powder Bed IR Heating System

In polymer LPBF, the material must be preheated to a level between the material's cooling and melting onset temperatures before the laser exposure [14]–[16]. State-of-the-art infrared heating uses a single sensor measurement to regulate the average powder-bed temperature but has no control over temperature distribution [8], [9].

This paper proposes a novel multi-zone closed-loop heating design that controls the build surface temperature profile. The IR heater above the powder bed (Fig. 2 and 3(a)) heats the powder bed via thermal radiation from nine independent heating zones (Fig. 3(b)). Each zone is composed of one or two quartz tube heaters. The radiation power for different zones

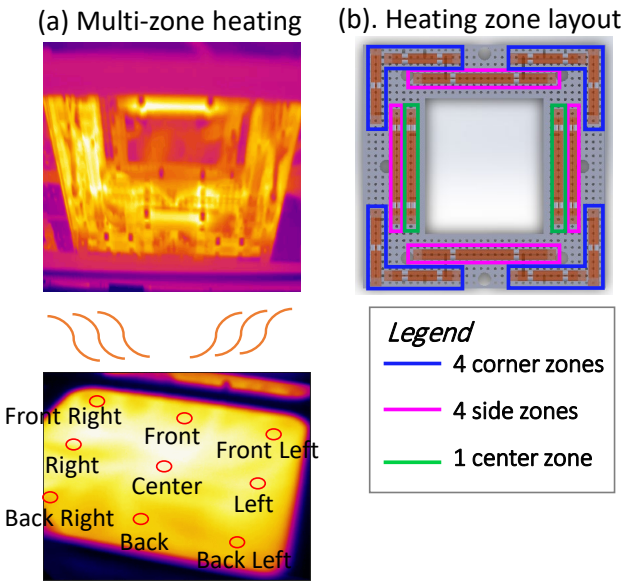

Fig. 3. Proposed powder bed temperature control system. (a) Illustration of the multi-zone infrared heating process. (b) Heating zone layout of the multi-zone infrared heater.

can be separately controlled using a 16-channel analog voltage output DAC (digital-to-analog converter).

The temperature measurement can be obtained from either a pyrometer or an infrared camera. The pyrometer measures the average temperature of an area on the powder surface. The infrared camera, on the other hand, provides a spatially resolved thermal profile with a resolution of 320 pixel × 240 pixel at a frame rate up to 60 Hz. In the captured image, we sample the temperature at nine locations (Fig. 3(a)) and use the measurements to control the nine heating zones of the IR heater, which will be discussed in detail in Section III.

B. Coaxial In-process Monitoring System

The in-process monitoring system exploits a coaxial optical configuration, where the imaging optical axes are shared with the laser beam. This configuration enables the acquisition of high lateral resolution images of melt pool dynamics and is widely used in LPBF monitoring studies [17], [18].

The camera employed on the developed platform is a monochrome visible light camera that provides more than 2,000 frames per second at a full resolution of 1920 pixel × 1080 pixel. A higher framerate is possible by reading from only a smaller region of interest. The camera is triggered by an FPGA (Field-Programmable Gate Array)-based frame grabber. After acquisition, the data is processed by the FPGA. The results (e.g., process signatures, defect formation dynamics) are then transferred to the host computer, which controls the process parameters through a real-time control (RTC) board. The computer also parses the scanning vectors and collects motion data for the two galvo scanner axes. These data, including part, layer, scan parameter, scan vector types, direction, and other vector metadata, can be synchronized with captured imaging data.

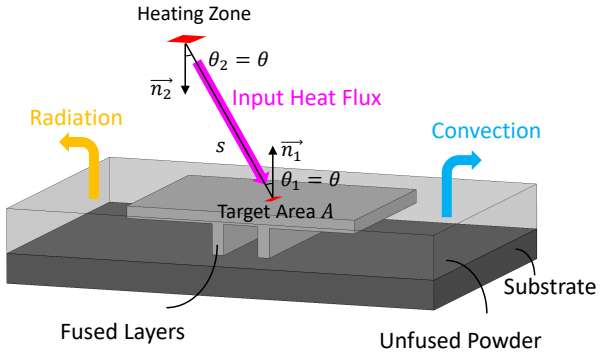

Fig. 4. Schematic illustration of the thermal processes during infrared preheating.

III. Powder Bed Temperature Control

In this section, we elaborate on the multi-zone powder bed temperature control method.

A. Multi-zone IR Heating Model

Fig. 4 illustrates the thermal processes involved in preheating materials in LPBF. Consider a small target area A on the powder bed with the thickness of one layer d. For the targeted controls, the thermal conduction of the polymer powder material is slow compared to the radiative and convective energy transfer. Therefore, the governing equation of the temperature $T(t)$ for this area is:

$$\rho d c_p \frac{\mathrm{d}T(t)}{\mathrm{d}t} = q + h_c \left[T_e - T(t)\right] + \varepsilon \sigma_B \left[T_e^4 - T^4(t)\right], \quad (1)$$

where the relevant parameters are described in Table II. The right-hand side of (1) characterizes the heat flux from the heating zone, the convection, and the radiation with the environment. Assuming that the IR radiation power of the heating zone is u, the heat flux can be expressed as

$$q = F \varepsilon u, \quad (2)$$

where ε is the emissivity and the F is the view factor, which can be modeled as

$$F = \frac{\cos\theta_1 \cos\theta_2}{\pi S^2} = \frac{\cos^2\theta}{\pi S^2}, \quad (3)$$

where θ_1 and θ_2 are the angles between the surface normals ($\vec{n}_1$ and $\vec{n}_2$ in Fig. 4) and a ray between the target area A on the powder bed and the heating zone, S is the distance between them. Because the heater is parallel with the powder bed, we have $\vec{n}_1 \parallel \vec{n}_2$ and $\theta_1 = \theta_2 = \theta$.

Fig. 4 shows the thermal process when there is only one heating zone and one target area. Next we extend to n heating zones and m target areas to create the state-space model of the multi-zone IR heating process.

TABLE II
PARAMETERS OF POWDER BED HEAT TRANSFER GOVERNING EQUATION

Parameter	Description	Unit
ρ	powder density	$\mathrm{kg/m^3}$
c_p	specific heat capacity	$\mathrm{J/kg/K}$
d	layer thickness	m
h_c	convection heat transfer coefficient	$\mathrm{W/m^2/K}$
ε	emissivity	n/a
σ_B	Stefan-Boltzmann constant	$\mathrm{W/m^2/K^4}$
q	input heat flux from a heating zone	$\mathrm{W/m^2}$
T_e	ambient temperature	K

Consider a target area $i \in \{1, 2, \ldots, m\}$, when there are n heating zones, combining (1) and (2) gives the governing equation of this area

$$\rho d c_p \frac{\mathrm{d}T_i(t)}{\mathrm{d}t} = \varepsilon \begin{bmatrix} F_{1i} & F_{2i} & \cdots & F_{ni} \end{bmatrix} \begin{bmatrix} u_1(t) \\ u_2(t) \\ \vdots \\ u_n(t) \end{bmatrix} + h_c \left[T_e - T_i(t)\right] + \varepsilon\sigma_B \left[T_e^4 - T_i^4(t)\right], \tag{4}$$

where $T_i(t)$ is the temperature of area i, $F_{1i},\ F_{2i}, \ldots,\ F_{ni}$ are the view factors between n heating zones and the area i, and $u_1(t),\ u_2(t), \ldots,\ u_n(t)$ are the radiation powers of the heating zones.

Note that (4) is a non-linear ordinary differential equation. With a working temperature (or set-point preheating temperature) T_0, the linearization of the nonlinear term is $T_i^4(t) = T_0^4 + 4T_0^3\left[T_i(t) - T_0\right]$. Organizing and extending (4) to m target areas on the powder bed, we obtain the following n input m output state-space linear approximation model

$$\begin{aligned} \frac{\rho d c_p}{k_1}\frac{\mathrm{d}}{\mathrm{d}t}\begin{bmatrix} \tilde{T}_1(t) \\ \tilde{T}_2(t) \\ \vdots \\ \tilde{T}_m(t) \end{bmatrix} &= I \begin{bmatrix} \tilde{T}_1(t) \\ \tilde{T}_2(t) \\ \vdots \\ \tilde{T}_m(t) \end{bmatrix} + \varepsilon \begin{bmatrix} F_{11}F_{21}\cdots F_{n1} \\ F_{12}F_{22}\cdots F_{n2} \\ \vdots\ \vdots\ \ddots\ \vdots \\ F_{1m}F_{2m}\cdots F_{nm} \end{bmatrix} \begin{bmatrix} u_1(t) \\ u_2(t) \\ \vdots \\ u_n(t) \end{bmatrix} \\ \begin{bmatrix} y_1(t) \\ y_2(t) \\ \vdots \\ y_m(t) \end{bmatrix} &= I \begin{bmatrix} \tilde{T}_1(t) \\ \tilde{T}_2(t) \\ \vdots \\ \tilde{T}_m(t) \end{bmatrix}, \end{aligned} \tag{5}$$

where $\tilde{T}_i(t) = k_1 T_i(t) + k_2$, $T_i(t)$ is the affined temperature of the target area i, I is an $m \times m$ identity matrix, F_{ji} is the view factor between heating zone j and target area i, $k_1 = -(h_c + 4\varepsilon\sigma_B T_0^3)$, and $k_2 = h_c T_e + \varepsilon\sigma_B T_e^4 + 3\varepsilon\sigma_B T_0^4$.

B. Multi-zone Heating Control

In this paper, we propose a suboptimal multi-zone control design based on a decoupled form of the MIMO model (5). Specifically, we select the temperature sampling areas in Fig. 3(a) such that the area i is right under the heating zone i. In other words, the view facor angle θ in equation (3) between the area i and the heating zone i is 0. Such a layout makes the diagonal entries of the view factor matrix in (5) one or two orders of magnitude larger than the off-diagonal entries. Therefore, we can drop the off-diagonal entries and approximate the full-order equation (5) with a decoupled model[2]

$$\frac{\rho d c_p}{k_1}\frac{\mathrm{d}}{\mathrm{d}t}\begin{bmatrix} \tilde{T}_1(t) \\ \tilde{T}_2(t) \\ \vdots \\ \tilde{T}_9(t) \end{bmatrix} = I \begin{bmatrix} \tilde{T}_1(t) \\ \tilde{T}_2(t) \\ \vdots \\ \tilde{T}_9(t) \end{bmatrix} + \frac{\varepsilon}{\pi h^2} \begin{bmatrix} 1 & 0 & \cdots & 0 \\ 0 & 1 & \cdots & 0 \\ \vdots & \vdots & \ddots & \vdots \\ 0 & 0 & \cdots & 1 \end{bmatrix} \begin{bmatrix} u_1(t) \\ u_2(t) \\ \vdots \\ u_9(t) \end{bmatrix}, \tag{6}$$

where h is the nominal distance between the IR heater and powder bed surface.

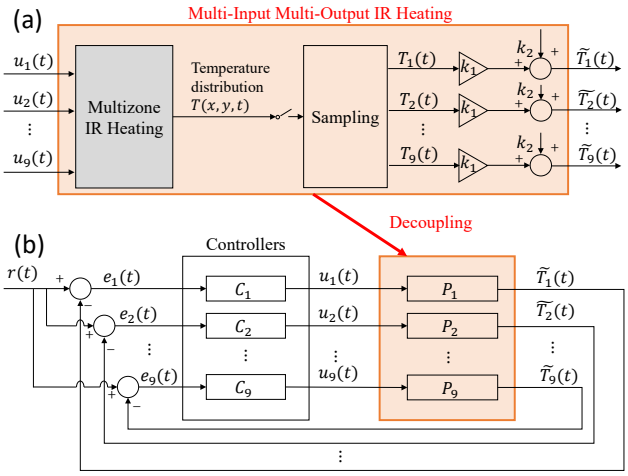

Fig. 5. Block diagram of the proposed multi-zone powder bed heating control. (a) multi-input Multi-output IR heating model. (b) Control design utilizing the decoupled IR heating model.

Fig. 5 shows the multi-zone control block diagram. Fig. 5(a) illustrates the multi-input multi-output IR heating model described by (5). The decoupled form based on (6) are nine independent first-order plants $P_1(s),\ P_2(s),\ \ldots,\ P_9(s)$, where the transfer function $P_i(s)$ is

$$P_i(s) = \frac{\varepsilon}{\pi h^2}\frac{k_1}{-k_1 + \rho d c_p s} \tag{7}$$

Therefore, the proposed multi-zone control is to use nine individual controllers $C_1,\ C_2,\ \ldots,\ C_9$ to regulate the affined temperatures $\tilde{T}_1(t),\ \tilde{T}_2(t),\ \ldots,\ \tilde{T}_9(t)$ based on the reference $r(t)$. Upon convergence, the error signals $e_i(t),\ e_j(t) \to 0$ and $\Delta_{ij} \triangleq \tilde{T}_i(t) - \tilde{T}_j(t) \to 0$, for $\forall i, j \in \{1, 2, \ldots, 9\}, i \neq j$. In other words, the multi-zone control minimizes the temperature gradient across the powder bed by minimizing the temperature difference among the sampling points.

C. Heating Experiment Verification

We verified the proposed method in the experiment of Polyamide 12 (PA12, a.k.a. Nylon 12) preheating. We considered different stages of fabrication and the impact of part-geometry-induced thermal disturbance. Fig. 6 shows three different temperature profiles of the powder bed surface plane. They were measured after a new layer of powder material was spread across the powder bed (step 2 in Fig. 1(a)) and before

[2]Recall Section II-A. We have nine heating zones and nine sampling points in the developed platform. Therefore, we have $m = n = 9$.

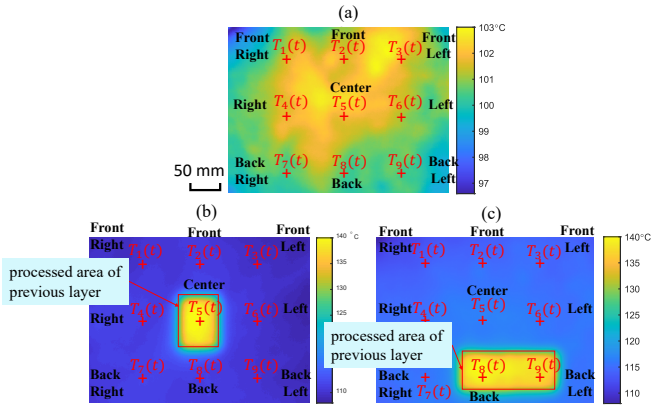

Fig. 6. Illustration of different thermal profiles before preheating starts. (a) Initial layer of the part. (b) Previously fused layer is around the center. (c) Previously fused layer is around the back corner.

the preheating started. Fig. 6(a) corresponds to the initial layer of the printing and there is only loose powder/build plate below the new powder layer. Fig. 6(b) and 6(c) can either represent two different layers/stages of the same part or two parts with different geometries[3]. The previously processed areas are seen to have a higher temperature than the surrounding unprocessed area, which creates a part-geometry-induced interlayer thermal disturbance. The impacted area is around the center in Fig. 6(b), and around the backleft area in Fig. 6(c).

The proposed multi-zone control was tested for preheating the powder bed with the three initial thermal profiles in Fig. 6. The performance is additionally compared against two representative controls. The design details for all three controllers are described below.

Model predictive control: We applied a multivariable MPC that utilizes the full-order MIMO heating process model (5) and calculates a sequence of future control actions (control horizon) such that a cost function over the prediction horizon is minimized. The MPC is implemented via the National Instruments Inc LabVIEW® predictive control toolkit. The development of the toolkit follows [19], which is based on generalized predictive control (GPC) detailed in [20], [21].

The MPC implementation was realized via the steps below:

1) We first preheated the powder bed to the working temperature 150 °C and then stimulated all heating zones with PRBS (pseudorandom binary sequence) signals. With the input and measured temperature output data, we identified the parameters in (5) with the Matlab system identification toolbox.
2) Based on the identified model, we measured the step response and obtained the average rise time.
3) With the rise time, we set the sampling time, prediction horizon, and control horizon of the MPC based on empirical design rules and computation complexity. For example, the sampling time was selected such that we fit 20 samples within the rise time.
4) We chose the output error weightings, control action error weightings, and control change rate weightings based on their relative significance. In this problem, the latter two are less important and thus have much lower weightings compared with the output error.
5) The tuning results are shown in Table III. With the identified model and the design parameters, we obtained the MPC controller in LabVIEW®, which was then used to control the powder-bed temperature.

[3]We tested two parts at different locations in this study.

TABLE III
TUNED MPC PARAMETERS [20]

Sampling Time T_S (s)	Prediction Horizon N_P	Control Horizon N_C	Control Change Rate Weightings R
1	30	12	$0.1\times I_{9\times 9}$
Output Error Weightings Q	**Control Error Weightings N**	**Control Action Limit (V)**	**Output Limit (°C)**
$I_{9\times 9}$	$0.1\times I_{9\times 9}$	0 - 4.5	100 - 170

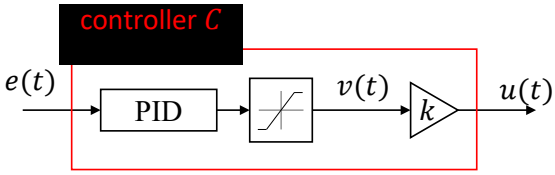

Fig. 7. Schematic of the controller in multi-zone and single-loop control.

Multi-zone control: As shown in Fig. 5(b), the multi-zone control is composed of nine separate closed loops for nine heating zone-sample point pairs. The schematic of the controller for each loop is illustrated in Fig. 7. It is composed of an anti-windup PID controller, a saturation, and a heating gain. The PID controller has the transfer function $K_p(1 + \frac{1}{T_i s} + T_d s)$, where K_p, T_i, and T_d are the proportional gain, integral time, and derivative time, respectively. The saturation limits the voltage output $v(t)$ of the heating power control DAC to the range of $[0,\ 4.5]$ V. The PID controller uses an integral sum correction algorithm to facilitate the anti-windup design [22]. The power regulation circuit of each heating zone is modeled as a gain k that transfers the control voltage $v(t)$ to IR radiation power $u(t)$. The PID gains are tuned with Ziegler-Nichols method and provided in Table IV. The proportional gains of different heating zones are inversely correlated with the power regulation circuit gains. The integral time and derivative time are set as identical for all heating zones because their periods of oscillation are close. The sampling time of the PID controllers is 0.2 s.

Single-loop control: The average temperature over a large area is used as feedback, and all heating zones share the same control output from one controller – a state-of-the-art method in the current polymer LPBF process. In this study, we use the pyrometer signal to measure the average powder-bed temperature.

A controller with the same schematic in Fig. 7 is used for this method. The controller gains are $K_p = 13.21$, $T_i = 3.87$ s, and $T_d = 0.97$ s. Note that compared with that of multi-zone control, the oscillation time is higher because the control action is based on the common mode of all heating zones.

As a case study, we selected the temperature reference as

TABLE IV
PID CONTROLLER GAINS FOR MULTI-ZONE CONTROL

Heating Zone	K_p	T_i (sec)	T_d (sec)
Front Right	13.11	1.63	0.41
Front	15.22		
Front Left	13.41		
Right	11.15		
Center	8.29		
Left	11.45		
Back Right	13.11		
Back	15.82		
Back Left	13.41		

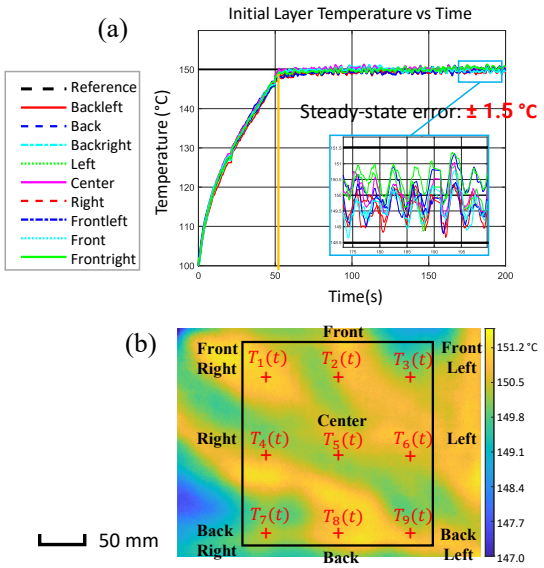

Fig. 8. Preheating result with multi-zone control for the initial layer. (a) Temperature evolution for all sampling locations. (b) Thermal profile of the powder bed at the steady state.

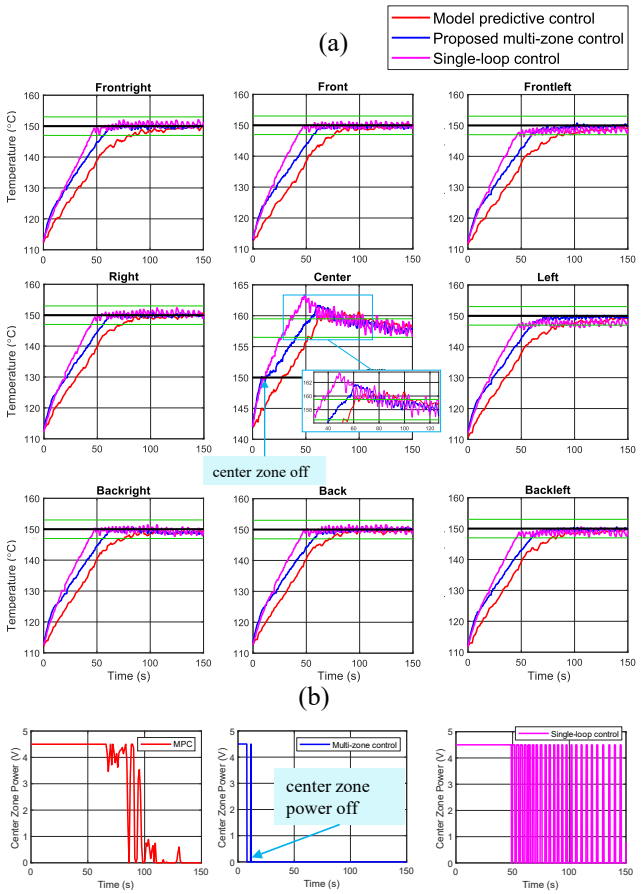

Fig. 9. Comparison of heating control algorithms. (a) Temperature evolution of the sampling locations on the powder bed. (b) Center zone heating power.

150 °C. This level was chosen such that we could evaluate the impact of worst-case interlayer thermal disturbance to compare the performance of the three control methods and, at the same time, avoid over melting caused by potential large temperature overshoot, especially for single-loop control.

Fig. 8 shows the heating result using the proposed multi-zone control when there is no cross-layer thermal disturbance (case in Fig. 6(a)). The temperature of all nine sampling points increased from 100 °C to the reference temperature 150 °C within 60 seconds. At the steady state, the temperature deviation is constrained within the envelope of $[148.5, 151.5]$ °C. Fig. 8(b) shows the powder-bed thermal profile at $t = 200$ s, where peak-peak temperature deviation within the box is less than 3 °C.

Fig. 9 shows the heating results using the three control schemes when the cross-layer thermal disturbance occurs around the center (Fig. 6(b)). Before the center zone temperature reached the reference (the time instance denoted by the arrow), both single-loop and multi-zone methods operated all heating zones with full power. MPC limited some control efforts of the non-center zones. After this point, the proposed control was able to effectively turn off the unnecessary center heating, as shown in Fig. 9(b). MPC reduced the power of the center zone gradually, and single-loop control continued to operate the center zone at full scale until all sampling locations reached the reference temperature.

As a result, the single-loop control, the multi-zone control, and MPC have heating speeds in descending order. The zoomed-in plot in Fig. 9(a) shows the peak temperature overshoots at the center zone. The multi-zone control and MPC have comparable peak errors. On the contrary, the single-loop control generated a much larger overshoot, which can potentially cause the powder to melt before laser exposure, in which case the fabrication has to be aborted.

At the steady state, the MPC, multi-zone control, and single-loop control lead to temperature deviations of 0.39 °C, 0.30 °C, and 0.76 °C across all heating zones, respectively. The steady-state performance of single-loop control is significantly inferior because, at each moment, the control action is not discrete for different locations of the powder bed.

When there are previously fused layers, as in the cases of Fig. 6(b) and 6(c), we propose an adaptive parameter tuning building on the multi-zone control. Specifically, as the geometry of the previous layer can be obtained from the CAD model, the location of the high-temperature area is available to the controller before the heating for the current layer starts. We can then limit the control power for the heating zones that fall in the predicted high-temperature area. Moreover, when

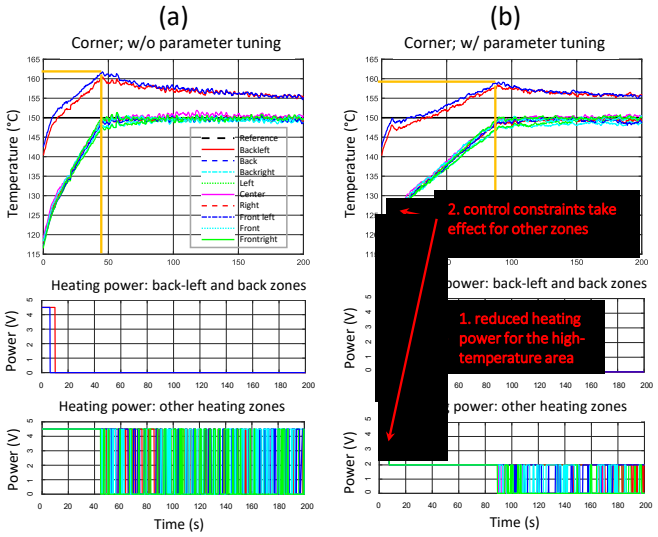

Fig. 10. Multi-zone control with interlayer thermal disturbance around backleft area. (a) Baseline case without add-on parameter tuning. (b) With add-on tuning.

the temperature of these zones reaches the reference point, we further limit the control power of other heating zones to mitigate the impact of the latent heat.

Fig. 10 illustrates this adaptive preheating process for the initial thermal profile in Fig. 6(c). The interlayer thermal disturbance was around the backleft corner. Therefore, the power control of the backleft and back zones was reduced from 4.5 V to 2 V from $t = 0^-$ s. After 10 s, the temperature of the back area reached the reference temperature, the algorithm further limited the power control of other heating zones to 2 V. As a result, compared with the baseline case (Fig. 10(a)), this adaptive parameter tuning reduced the peak temperature error from 12 °C to 9 °C.

In summary, in this section, we propose a control-oriented MIMO IR heating model. Based on the full-order and decoupled form MIMO model, we demonstrated comparable results of an MPC method and an in-house developed multi-zone heating method. The advantages of the MPC formulation are adjustable constraints and centralized consideration of different heating zones under an optimization framework. Such a model-based configuration is recommended when the parameters in model (5) can be accurately identified. The advantages of the formulated multi-zone control are direct control of individual heating zones, flexibility for parameter tuning to accommodate different initial thermal conditions, and design for robustness. Such a formulation is recommended when designers have a good engineering understanding of the system dynamics and/or when the physical process contains uncertainties and time-varying dynamics.

IV. Low-Contrast Imaging Data Analytics

With the sensing and controls to assure proper material conditions before the laser irradiation, this section discusses the in-situ monitoring and data analytics framework for the signature dynamics in the laser-material interaction area. Along with this process, we propose a data processing

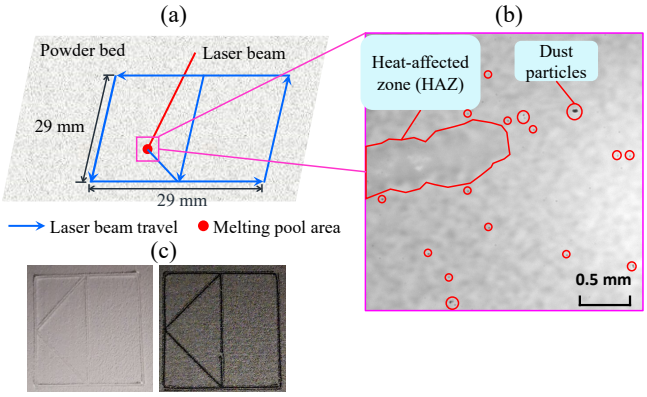

Fig. 11. Experiment setup. (a) Schematic diagram of fusion geometry. (b) Raw image example. (c) Solidified geometry with light- and dark-color materials.

analytics framework that (1) addresses salient challenges in the raw image when the temperature gradient is low between the laser-heat affected zone and the surrounding materials, (2) collects defect formation dynamics related to material melting and solidification, and (3) provides important process signatures (e.g., melt pool width).

We verified this framework in a benchmark printing experiment on the developed platform. As shown in Fig. 11, we monitored the melt pool area when processing a geometry that is composed of a square and a triangle. Both light- and dark-color PA12 materials were tested.

A. Preprocessing for image enhancing

In a typical in-situ collected image (Fig. 11(b)), several salient challenges exist that hinder data interpretation:

- noise due to optical path contamination, characterized by small yet dark particles,
- uneven background intensity: e.g., the right part of the image is brighter than the left because of inconsistent illumination, and
- low contrasts between the processed zone and the surrounding loose powder.

We propose to utilize a combination of pre-processing algorithms to address these issues. We use morphological image processing to remove the dust particle noises. Most morphological algorithms involve a combination of set operations between image f and structuring elements (SEs)—shapes used to probe an image understudy for properties of interest. The specific algorithm we propose to use here is grayscale closing [23]. The effect of this operation is to attenuate the small and dark features in f while keeping the bright details and background relatively intact. Fig. 12(b) shows the results of applying grayscale closing on the raw image with a disk SE diameter of 17 pixels. Except for one dust particle larger than the SE, all particle noises are successfully removed. Meanwhile, the profile and texture of the laser-processed zone remain unaffected. Next, we use flat-field correction (FFC) to compensate for the uneven illumination in the raw image. The algorithm creates a flat-field image that represents the background intensity [24].

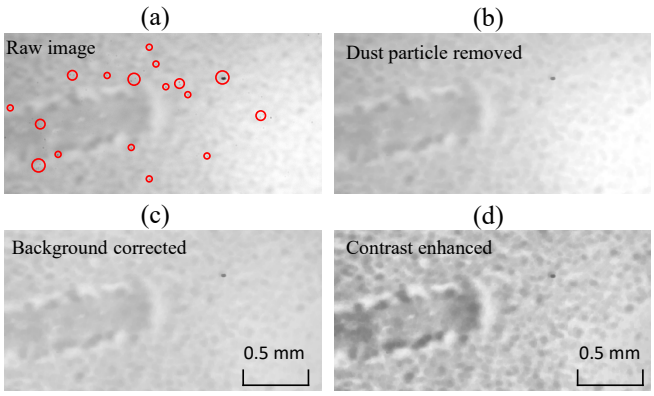

Fig. 12. Pre-processing results with proposed algorithms. (a) Raw noisy image. (b) Remove dust particle noises with grayscale closing. (c) Improve background intensity with flat-filed correction. (d) Enhance contrast using CLAHE.

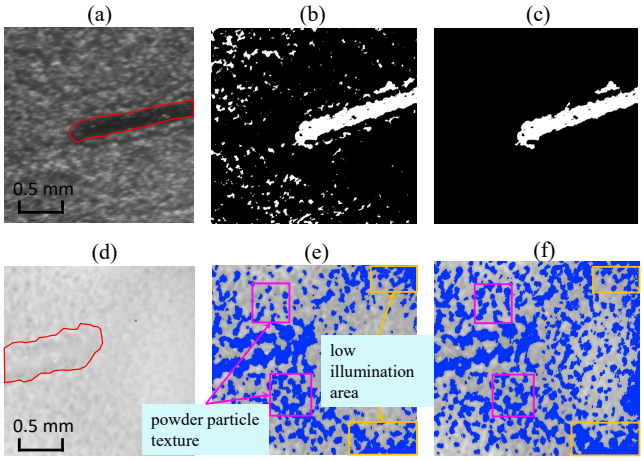

Fig. 13. Processed zone identification with simple thresholding algorithm. (a) Captured image for dark-color PA12. (b) Global-thresholding of (a). (c) Morphological opening of (b). (d) Captured image for light-color PA12. (e) Global-thresholding of (d). (f) Local thresholding of (d).

With the estimated flat-field image, each original image pixel is adjusted. As a result, the background intensity of the corrected image distributes evenly across the whole image, as shown in Fig. 12(c). We then apply contrast limited adaptive histogram equalization (CLAHE) [25], to improve the local contrast around the boundary of the processed zone and enhance the edges' definitions. As viewed in Fig. 12(d), in the enhanced image, CLAHE increases the grayscale-level difference between the laser-processed and unprocessed zones, which is beneficial for the following segmentation algorithm discussed in Section IV-B.

Both grayscale closing and CLAHE have a computational complexity of $O(n)$ for an image with n pixels using efficient implementation methods [26], [27]. Therefore, they are suitable for online analysis. With a flat-field image, the complexity of FFC is also $O(n)$. There are two methods to estimate the flat-field image. One method is to fit a mathematical model on the target image intensity. This is performed on a sampled grid of pixels and the complexity is substantially high. The second is to measure a dark image and a flat image of the field of view using the camera. For online implementation, it is recommended to use the second method to obtain the flat-field image before printing. In this study, the image processing was performed offline and the first method was implemented.

B. Heat-affected zone identification

Identification of the melt pool and the heat-affected zone is necessary to understand the complex laser-material interactions. However, this is challenging for materials such as light-color polymer. When subject to laser radiation, the grayscale levels for the processed and the unfused powder are similar, and the simple threshold-based binarization algorithm is insufficient to distinguish them. As illustrated in Figs. 13(a)-(c), for dark-color polymer, the processed zone can be isolated using thresholding and morphological processing. However, for light-color polymer (e.g., white PA12, white PEEK), the grayscale level of the processed zone varies wildly. The observed feature also overlaps with pixels of unprocessed powder and lightly illuminated regions (corners in Fig. 13(e) and 13(f)). CLAHE mitigates such an overlap. However, neither global nor local thresholding is effective enough to separate different zones. Therefore, for light-color polymer, we need a more effective identification algorithm.

The technique we propose to identify the processed zone is an efficient graph-based image segmentation [28]. In this algorithm, the original image is transformed into a graph $G = (V, E)$, where each node $v_i \in V$ corresponds to a pixel in the image, and the edges $(v_i, v_j) \in E$ connect certain pairs of neighboring pixels. A weight $w((v_i, v_j))$ is associated with each edge, which is defined as the absolute grayscale difference between elements v_i and v_j. Using this representation, the algorithm then defines a predicate for measuring the evidence for a boundary between two regions. Based on this predicate, the segmentation can be created by pairwise region comparison. The method runs in $O(n \log n)$ time for n image pixels and generally runs in a fraction of a second on an average desktop computer for a 320 pixel × 240 pixel image in the offline processing. Leveraging the parallel computation advantage of the FPGA, the execution time is expected to be reduced to milliseconds.

Fig. 14 illustrates the result of the proposed zone identification with graph-based segmentation. After preprocessing (Fig. 14(b)) and segmentation, the original image is divided into five components (annotated by five colors) in Fig. 14(c). Recall that the imaging data is synchronized with the scan data (Section II-B). The light blue component thus depicts the processed zone as it overlaps with the current scan vector. Note that the bilateral boundaries of the processed zone are accurately identified along the scan direction. However, the front edge of the melt pool is not found from the synchronized image because the melt pool area has not solidified yet and the grayscale-level difference with surrounding powder is minimal (it is difficult to identify this edge even with human perception). Nevertheless, we can estimate this edge *a priori* by combining the location of the melt pool center and the estimated diameter of the melt

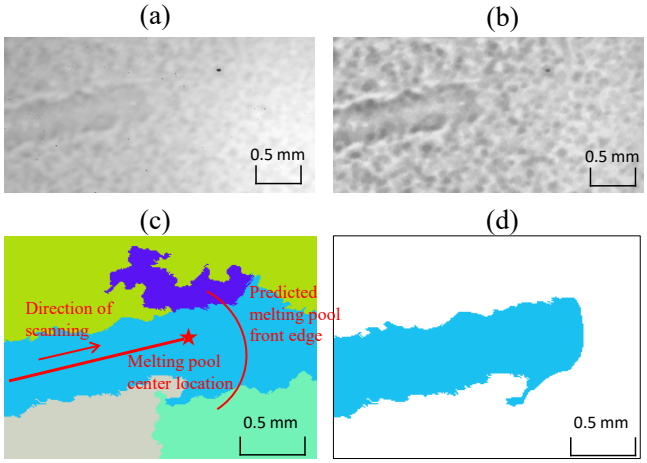

Fig. 14. Proposed zone identification with graph-based segmentation. (a) Raw image. (b) Pre-processed image. (c) Segmentation result. (d) Identified processed zone.

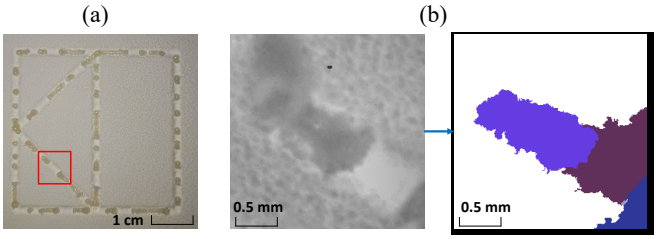

Fig. 15. Excessive heating defect detection. (a) Processed zone with discontinuities. (b) Segmentation result of the red box area in (a).

pool. The former is fixed in each image frame as a benefit of the coaxial optical design. The latter can be obtained by calculating the processed zone width in the previous frame. Using this estimated edge to split the component, we can accurately extract the processed zone (Fig. 14(d)) from the original noisy and low-contrast raw image.

C. Defect detection and process signatures extraction

Based on the identification result, we can further detect various defects. For example, Fig. 15 illustrates an excessive heating defect, which can result from abnormal printing parameters or challenging part structures (e.g., down-facing overhang surface). When this happens, the solidification rate of the melt pool is too high, which causes the processed zone discontinuities. Fig. 15(b) shows the segmentation result for the image captured at the location denoted by the red box in Fig. 15(a). We see that in the segmented image, the discontinuity is flagged by multiple components along the path of the scanning vector. When such a defect is detected, an in-process controller can either modify the printing parameters or abort the printing.

The image analytics framework can also provide process signatures that correlate to the part quality metrics. For example, the melt pool width of each frame can be estimated by calculating the ratio between the component size in Fig. 14(d) and the scan vector length in Fig. 14(c). The result, after filtering (with e.g., Kalman filter [29]), could be used as a feedback for closed-loop control. In [30], we proposed two quantitative process signatures based on the segmentation result, specifically (1) the ratio between the component perimeter and the scan vector length and (2) width variance along the laser traveling direction. We showed there that these features correlate with the delivered laser energy density.

V. Conclusion and Future Work

In this paper, we presented (1) a model-based multi-zone heating control method for minimizing the powder-bed temperature deviation in the presence of part-geometry induced cross-layer thermal disturbance and (2) an image analytics framework for process monitoring of low melt pool contrast material LPBF using visible light cameras. We compared three powder preheating controller designs and revealed the benefits of different algorithms. Leveraging multiple image processing algorithms, the image analytics framework identifies the laser-processed area and provides process signatures based on visible light camera data, which is a missing piece in the literature on monitoring the LPBF process of low-contrast materials such as light-color polymer.

In this paper, the proposed image analytics framework was developed and verified offline using captured image database. Further work includes implementing the framework on the FPGA frame grabber on the fly, data analytics, and controls with the extracted process signatures.

Acknowledgement

This work is supported in part by NSF Award 1953155 and a GE fellowship for innovation. Any opinions expressed herein are those of the authors and do not represent those of the sponsors.

References

[1] M. Mani, S. Feng, B. Lane, A. Donmez, S. Moylan, and R. Fesperman, "Measurement science needs for real-time control of additive manufacturing powder bed fusion processes," Natl. Inst. Stand. Technol., Gaithersburg, MD, NIST Interagency/Internal Report (NISTIR) 8036, 2015.

[2] T. G. Spears and S. A. Gold, "In-process sensing in selective laser melting (SLM) additive manufacturing," *Integr. Mater. Manuf. Innov.*, vol. 5, no. 1, pp. 16–40, 2016.

[3] M. Grasso and B. M. Colosimo, "Process defects and in situ monitoring methods in metal powder bed fusion: a review," *Meas. Sci. Technol.*, vol. 28, no. 4, p. 044005, 2017.

[4] N. Gupta, C. Weber, and S. Newsome, "Additive manufacturing: status and opportunities," Sci. Technol. Polic. Inst., Washington, DC, USA, 2012.

[5] W. E. Frazier, "Metal additive manufacturing: a review," *J. Mater. Eng. Perform.*, vol. 23, no. 6, pp. 1917–1928, 2014.

[6] ——, "Direct digital manufacturing of metallic components: vision and roadmap," in *2010 Annu. Int. Solid Freeform Fabr. Symp.*, Austin, TX, USA, 2010, pp. 9–11.

[7] X. Chen, T. Jiang, D. Wang, and H. Xiao, "Realtime control-oriented modeling and disturbance parameterization for smart and reliable powder bed fusion additive manufacturing," in *2018 Annu. Int. Solid Freeform Fabr. Symp.*, Austin, Texas, USA, 2018.

[8] T. T. Diller, R. Sreenivasan, J. Beaman, D. Bourell, and J. LaRocco, "Thermal model of the build environment for polyamide powder selective laser sintering," in *2010 Annu. Int. Solid Freeform Fabr. Symp.*, Austin, Texas, USA, 2010.

[9] A. Wegner and G. Witt, "Process monitoring in laser sintering using thermal imaging," in *2011 Annu. Int. Solid Freeform Fabr. Symp.*, Austin, Texas, USA, 2011, pp. 8–10.

[10] L. Han, F. W. Liou, and S. Musti, "Thermal behavior and geometry model of melt pool in laser material process," *J. Heat Transfer*, vol. 127, no. 9, pp. 1005–1014, 2005.

[11] J.-P. Kruth, P. Mercelis, J. Van Vaerenbergh, and T. Craeghs, "Feedback control of selective laser melting," in *Virtual and Rapid Manufacturing*, 1st ed., London, United Kingdom: CRC Press, 2007, pp. 521–527.

[12] A. Shkoruta, S. Mishra, and S. J. Rock, "Real-time image-based feedback control of laser powder bed fusion," *ASME Lett. Dyn. Sys. Control*, vol. 2, no. 2, 2022.

[13] J.-P. Kruth, P. Mercelis, J. Van Vaerenbergh, L. Froyen, and M. Rombouts, "Binding mechanisms in selective laser sintering and selective laser melting," *Rapid Prototyp. J.*, vol. 11, no. 1, pp. 26–36, 2005.

[14] S. Greiner, K. Wudy, L. Lanzl, and D. Drummer, "Selective laser sintering of polymer blends: bulk properties and process behavior," *Polym. Test.*, vol. 64, pp. 136–144, 2017.

[15] M. Schmid and K. Wegener, "Additive manufacturing: polymers applicable for laser sintering (LS)," *Procedia Eng.*, vol. 149, pp. 457–464, 2016.

[16] I. Gibson, D. W. Rosen, B. Stucker, M. Khorasani, D. Rosen, B. Stucker, and M. Khorasani, *Additive Manufacturing Technologies*. Cham, Switzerland: Springer, 2021.

[17] T. Craeghs, F. Bechmann, S. Berumen, and J.-P. Kruth, "Feedback control of layerwise laser melting using optical sensors," *Phys. Procedia*, vol. 5, pp. 505–514, 2010.

[18] S. Fish, J. C. Booth, S. T. Kubiak, W. W. Wroe, A. D. Bryant, D. R. Moser, and J. J. Beaman, "Design and subsystem development of a high temperature selective laser sintering machine for enhanced process monitoring and control," *Addit. Manuf.*, vol. 5, pp. 60–67, 2015.

[19] L. Balbis, R. Katebi, and R. Dunia, "Graphical based predictive control design," in *Proc. 2005 IEEE Conf. Control Appl.*, Toronto, Canada, 2005, pp. 297–302.

[20] D. Clarke, C. Mohtadi, and P. Tuffs, "Generalized predictive control-Part I. The basic algorithm," *Automatica*, vol. 23, no. 2, pp. 137–148, 1987.

[21] A. W. Ordys and D. W. Clarke, "A state-space description for GPC controllers," *Int. J. Syst. Sci.*, vol. 24, no. 9, pp. 1727–1744, 1993.

[22] G. C. Goodwin, S. F. Graebe, M. E. Salgado *et al.*, "Classical PID control," in *Control System Design*, Upper Saddle River, NJ, USA: Pearson Prentice Hall, 2001.

[23] R. C. Gonzales and R. E. Woods, *Digital Image Processing*. Upper Saddle River, NJ, USA: Pearson Prentice Hall, 2002.

[24] J. A. Seibert, J. M. Boone, and K. K. Lindfors, "Flat-field correction technique for digital detectors," in *Medical Imaging 1998: Physics of Medical Imaging*, vol. 3336, Bellingham, WA, USA: International Society for Optics and Photonics, 1998, pp. 348–354.

[25] K. Zuiderveld, "Contrast limited adaptive histogram equalization," in *Graphics Gems*, Boston, MA, USA: AP Professional, 1994, pp. 474–485.

[26] P. Dokládal and E. Dokladalova, "Computationally efficient, one-pass algorithm for morphological filters," *J. Vis. Commun. Image Represent.*, vol. 22, no. 5, pp. 411–420, 2011.

[27] T. Sund and A. Møystad, "Sliding window adaptive histogram equalization of intraoral radiographs: effect on image quality," *Dentomaxillofac. Radiol.*, vol. 35, no. 3, pp. 133–138, 2006.

[28] P. F. Felzenszwalb and D. P. Huttenlocher, "Efficient graph-based image segmentation," *Int. J. Comput. Vis.*, vol. 59, no. 2, pp. 167–181, 2004.

[29] T. Jiang, M. Leng, and X. Chen, "Control-oriented mechatronic design and data analytics for quality-assured laser powder bed fusion additive manufacturing," in *2021 IEEE/ASME Int. Conf. Adv. Intell. Syst. Comput.*, 2021, pp. 1319–1324.

[30] ——, "Control-oriented in situ imaging and data analytics for coaxial monitoring of powder bed fusion additive manufacturing," in *Progress in Additive Manufacturing 2020*, West Conshohocken, PA: ASTM International, 2022, pp. 193–207.

Tianyu Jiang received the B.S. Degree from University of Science and Technology of China, Hefei, China in 2014, and the Ph.D. degree in mechanical engineering from the University of Washington, Seattle, WA, USA, in 2021. His research interests include theory and practice of dynamic systems and controls with application to additive and advanced manufacturing.

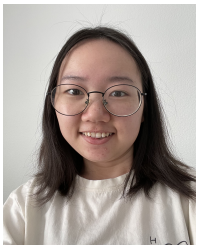

Mengying Leng received B.S. degree in Mechanical Engineering from Tsinghua University, China in 2019 and M.S. degree in Mechanical Engineering from the University of Seattle, WA, USA, in 2021. Her current research interest is vision-based robot control.

Xu Chen received the bachelor's degree (Hons.) from Tsinghua University, China, in 2008, and the M.S. and Ph.D. degrees in mechanical engineering from the University of California, Berkeley, CA, USA, in 2010 and 2013, respectively. He is currently an Associate Professor with the Department of Mechanical Engineering, University of Washington, Seattle, WA, USA. His current research interests include dynamic systems and controls, information fusion, advanced manufacturing, and intelligent machines. Dr. Chen is a recipient of the U.S. National Science Foundation CAREER Award, the SME Sandra L. Bouckley Outstanding Young Manufacturing Engineer Award, and the Young Investigator Award from the ISCIE/ASME International Symposium on Flexible Automation.